

Linear Response of Field-Aligned Currents to the Interplanetary Electric Field

Weimer, D. R. ; R. Edwards, T.; Olsen, Nils

Published in:
Journal of Geophysical Research

Link to article, DOI:
[10.1002/2017JA024372](https://doi.org/10.1002/2017JA024372)

Publication date:
2017

Document Version
Peer reviewed version

[Link back to DTU Orbit](#)

Citation (APA):
Weimer, D. R., R. Edwards, T., & Olsen, N. (2017). Linear Response of Field-Aligned Currents to the Interplanetary Electric Field. *Journal of Geophysical Research*, 122(8), 8502–8515 . DOI: 10.1002/2017JA024372

DTU Library

Technical Information Center of Denmark

General rights

Copyright and moral rights for the publications made accessible in the public portal are retained by the authors and/or other copyright owners and it is a condition of accessing publications that users recognise and abide by the legal requirements associated with these rights.

- Users may download and print one copy of any publication from the public portal for the purpose of private study or research.
- You may not further distribute the material or use it for any profit-making activity or commercial gain
- You may freely distribute the URL identifying the publication in the public portal

If you believe that this document breaches copyright please contact us providing details, and we will remove access to the work immediately and investigate your claim.

Linear Response of Field-Aligned Currents to the Interplanetary Electric Field

D. R. Weimer^{1,2}, T. R. Edwards¹, Nils Olsen³

Daniel Weimer, dweimer@vt.edu

¹Center for Space Science and
Engineering Research, Virginia Tech,
Blacksburg, Virginia, USA.

²National Institute of Aerospace,
Hampton, Virginia, USA.

³DTU Space, Technical University of
Denmark, Denmark.

This article has been accepted for publication and undergone full peer review but has not been through the copyediting, typesetting, pagination and proofreading process, which may lead to differences between this version and the Version of Record. Please cite this article as doi: 10.1002/2017JA024372

Abstract. Many studies that have shown that the ionospheric, polar cap electric potentials (PCEP) exhibit a “saturation” behavior in response to the level of the driving by the solar wind. As the magnitude of the interplanetary magnetic field (IMF) and electric field (IEF) increase, the PCEP response is linear at low driving levels, followed with a roll-over to a more constant level. While there are several different theoretical explanations for this behavior, so far no direct observational evidence has existed to confirm any particular model. In most models of this saturation, the interaction of the field-aligned currents (FAC) with the solar wind/magnetosphere/ionosphere system has a role. As the FAC are more difficult to measure, their behavior in response to the level of the IEF has not been investigated as thoroughly. In order to resolve the question of whether or not the FAC also exhibit saturation, we have processed the magnetic field measurements from the Ørsted, CHAMP, and Swarm missions, spanning more than a decade. As the amount of current in each region needs to be known, a new technique is used to separate and sum the current by region, widely known as R0, R1, and R2. These totals are found separately for the dawn and dusk sides. Results indicate that the total FAC has a response to the IEF that is highly linear, continuing to increase well beyond the level at which the electric potentials saturate. The currents within each region have similar behavior.

Keypoints:

- Field aligned currents have a linear response to the interplanetary electric field

- No saturation is observed for currents within any region or the total trans-polar current

- The combined solar wind and interplanetary magnetic field act as a current source

1. Introduction

The interaction of the solar wind with the Earth's magnetosphere results in the generation of electric fields and currents in the high-latitude, polar ionospheres. At low altitudes the currents flow into and out from the ionosphere along magnetic field lines. For a complete understanding of the solar-terrestrial interaction, it is necessary to know how the polar field-aligned currents (FAC) map in the ionosphere, and how they vary for different solar wind conditions.

The solar wind carries an embedded, interplanetary magnetic field (IMF), which in combination with the velocity of the plasma produces an electric field, known as the interplanetary electric field (IEF). This IEF is computed from the product of the velocity times the magnitude of the magnetic field in the perpendicular, Y-Z plane in Geocentric Solar Magnetic (GSM) coordinates. It is very well-known that the polar electric field exhibits a saturation effect. As the magnitude of the IEF driver increases the electric potential difference across the polar cap initially increases linearly, then the slope decreases until the potential levels off to a nearly constant value. This saturation is observed to occur at IEF values of 3 to 5 mV/m. This topic of electric potential saturation has been the subject of numerous publications in the past decade, and the debate over why it happens is yet unresolved [e.g. *Shepherd*, 2007, and references therein].

The purpose of this paper is to present results from an investigation of the response of the field-aligned currents to extreme driving conditions in the solar wind. The main objective is to answer the question of whether or not the FAC exhibit the same saturation behavior as shown in the electric potentials. As the solar wind/IMF conditions where the

saturation occurs are rare, a large number of measurements are required, gathered over a long time interval. We have satisfied this requirement by using data from magnetometer measurements on three missions (five satellites), Ørsted, Challenging Mini-satellite Payload (CHAMP), and the three Swarm satellites.

As described in more detail in Section 1.2, the FAC tend to occur within concentric belts, that are referred by a numbering sequence that indicates their order away from the pole. As the “Region 1” currents have a role in some of the saturation theories, we examine the amount of the current in each of these different regions or belts, rather than only the overall totals of the current. Taking advantage of a new ability to separate the FAC by region, we also report of the behavior of the different current regions as a function of the IMF clock angle, including the most poleward and ambiguous “Region 0.”

1.1. Saturation Theories

Borovsky et al. [2009] mentions nine models for polar-cap saturation from the literature, and examines their agreement to magnetohydrodynamic (MHD) simulations. In one model [*Hill et al.*, 1976; *Siscoe et al.*, 2002a, b] it is suggested that Region 1 (R1) currents reduce the dayside magnetic field and reduces the rate of dayside merging. The magnitude of the R1 current is limited to the level needed to balance the solar wind. *Siscoe et al.* [2004] point out that there are three other proposed saturation mechanisms that involve a limit on the strength of the R1 current system. In the past there has been no direct observational evidence exists to confirm one mechanism over another.

In the Alfvén wing model [*Ridley*, 2007; *Kivelson and Ridley*, 2008] the motion of the reconnected solar-wind plasma past the Earth acts as an MHD generator that couples to the ionosphere by means of field-aligned currents. They propose that “when the

impedance of the solar wind across open polar cap field lines dominates the impedance of the ionosphere, Alfvén waves incident from the solar wind are partially reflected, reducing the signal in the polar cap.” Thus, these currents are limited in strength by the “Alfvén conductance” of the solar-wind plasma. *Borovsky et al.* [2009] refer to this as the “MHD-Generator Model,” and their findings provided some support for this model, in that the total cross-polar-cap current (in MHD simulations) did not change significantly while the Pedersen conductance and electric potential drop varied. Their results implied that the cross-polar current is being driven by a generator that is current limited. But the Alfvén Mach number in the solar wind must be low (less than 4) for any effect to occur [*Ridley*, 2007].

In a newer force-balance model by *Lopez et al.* [2008], some of the Region 1 current flows on open field lines, where it exerts a $\mathbf{J} \times \mathbf{B}$ force on the solar wind pressure, leading to the saturation effect. Observations of FACs using magnetometers on the Defense Meteorological Satellite Program (DMSP) F13 satellite showed that when the IMF is strongly southward, a substantial amount of FAC was flowing on open magnetic field lines, the proportions being much greater than periods of nominal driving. Interestingly, the results by *Green et al.* [2009] appear to agree with this, as they show more of the R1 FAC being located on open field lines at larger levels of southward IMF.

The prior discussion about potential saturation only concerns southward IMF conditions. Electric potential saturation under northward IMF conditions has been studied also. *Wilder et al.* [2008] used SuperDARN radar measurements, finding that “the reverse convection cells do, in fact, exhibit non-linear saturation behavior. The saturation potential is approximately 20 kV and is achieved when the electric coupling function

reaches between 18 and 30 kV/ R_E ,” where R_E is the radius of the Earth. These values correspond to 2.8 – 4.7 mV/m, approximately the same limit as under southward IMF. *Sundberg et al.* [2009] also studied the saturation of the Northward B_Z (NBZ) system using DMSP F13 satellite drift meter measurements, rather than ground radar. They also found that the NBZ convection cells saturate, reaching a limit of about 60 kV. *Wilder et al.* [2009] expanded on their prior results, finding that the strength of the ionospheric electric field in the NBZ system under saturation is comparable to the electric field in the polar cap when the IMF is strongly southward. The dependence of the reverse convection potential on conductivity was found to be the opposite of what was expected. They found that the Alfvénic Mach number in the solar wind did not appear to be a fundamental driver of saturation.

The majority of the observational evidence on the saturation of the magnetosphere’s response to solar wind driving have used electric field measurements, usually with ground radar or satellite drift meters. Observational studies of the field-aligned currents in saturation conditions are rare. As mentioned earlier, the relationships between the currents and the electric potential saturation have been studied with MHD simulations. A common result in the majority of cases is that the Region 1 currents seem to have a role in the saturation of the electric potential, yet each study tends to produce a different explanation as to why. MHD simulations may also use values of ionospheric conductivity that are not entirely accurate. Obviously, actual measurements of the field-aligned currents in a variety of solar wind driving conditions will be very useful to helping to resolve this controversy over the causes of saturation.

The currents in the NBZ system also merit a closer look for conditions with high IMF magnitudes. *Stauning* [2002] had used Ørsted magnetometer measurements to derive the NBZ FAC patterns for IMF B_Z levels up to +20 nT, with the result that strong NBZ currents are seen only in the summer, and that the total FAC rises strongly above IMF $B_Z > 5$ nT. From the graphs shown by *Stauning* [2002] it is not clear if the total currents level out for IMF $B_Z > +10$ nT. Thus, it would be useful to extend these results to higher magnitudes of the IMF, and to determine how the FAC compares to the reversed convection cells in the electric potentials.

1.2. Field Aligned Current Mapping

An early work that pioneered the mapping of the FAC currents was by *Iijima and Potemra* [1976], whose schematic diagrams introduced the terminology “Region 1” for poleward belts of current, and “Region 2” for the lower-latitude belts. These bands of currents are prominent for strongly driven, two-cell convection patterns with a southward IMF (negative B_Z) driving. For strongly northward IMF (positive B_Z) the currents are found to have a pair of reversed-polarity FAC zones poleward of the Region 1 currents, sometimes referred to as the “NBZ” current system [*Iijima et al.*, 1984; *Zanetti et al.*, 1984; *Iijima and Shibaji*, 1987]. The electric potentials have a similar “NBZ” pattern consisting of a pair of reversed convection cells near the pole at noon, surrounded by a pair of larger cells having a normal, anti-sunward flow in the polar cap and sunward at lower latitudes [*Weimer*, 1995]. The most poleward FAC are also referred to as “Region 0,” and sometimes as B_Y currents due to their appearance when the IMF has a strong component in the Y direction.

The earliest FAC studies presented sketches of current sheets for a few generalized IMF orientations. Quantitative progress initially started with inversions of ground-based magnetometer measurements [*Friis-Christensen et al.*, 1985; *Lu et al.*, 1995]. Later on, methods were developed for deriving quantitative maps of the FAC distribution using magnetometer measurements on satellites. For example, *Papitashvili et al.* [2002] and *Christiansen et al.* [2002] used the curl of mapped magnetic perturbations, as did *Stauning* [2002], concentrating on the NBZ FAC patterns.

Weimer [2000] and *Waters et al.* [2001] introduced a method in which spherical harmonic fits were used to derive a magnetic Euler potential function from magnetometer data, from which the FAC are derived. Examples of results obtained by this method are shown by *Weimer* [2001] and *Weimer* [2005], using data from the Dynamics Explorer-2 satellite, while *Green et al.* [2006], *Anderson et al.* [2008], *Korth et al.* [2008], and *Green et al.* [2009] use data collected from the 79 Iridium satellites. With this same constellation, *Anderson and Korth* [2007] investigated the topic of current saturation, using measurements obtained during 66 intervals from 23 storms. They found a good linear fit to the response of the FAC to the IEF, up to 10 mV/m, with some evidence for current saturation in the widely scattered data points above this level.

2. Data Sources

The Ørsted, CHAMP, and Swarm satellites carried high-accuracy magnetometers for measuring Earth's magnetic field. During the course of their missions, these satellites sampled all local times and geomagnetic latitudes.

The Ørsted satellite was launched in February 1999 into an orbit inclined at 96.5°, having an initial altitude range of 650–860 km, and it obtained measurements up through

May 2011 [*Thomsen and Hansen, 1999; Olsen, 2007*]. Our magnetometer data from Ørsted spans the time period from 15 March 1999 to 26 August 2005.

The CHAMP satellite was launched in July 2000, having a close to circular orbit at 87° inclination. It had an initial altitude of 454 kilometers, and the mission lasted until September 2010 [*Reigber et al., 2002; Maus, 2007*]. The magnetometer data from CHAMP that we used begin on 15 May 2001, and ends on 2 September 2010.

The three, identical Swarm satellites were launched in November 2013, and have a design lifetime of at least 4.5 years [*Friis-Christensen et al., 2006; Olsen et al., 2013*]. Two of the satellites had an initial altitude of 450 kilometers, at an inclination angle of 87.4°, while the third launched at an altitude of 530 kilometers and maintained an 88° inclination. All Swarm satellites are still operational. After more than three years in space all three spacecraft and their payload show no sign of degradation, and the European Space Agency, responsible for Swarm, now plans for an extension of the mission for the next 10+ years.

The data from these five satellites were processed to remove the magnetic field due to Earth's internal sources, using the International Geomagnetic Reference Field (IGRF) model appropriate for the time period. As the data from each mission have different formats and coordinates, specifically tailored programs were required to process their data. The residual magnetic field is separated into two vector components in the plane that is perpendicular to the IGRF reference field. For simplicity we refer to the magnetic field difference as $\Delta\mathbf{B}$. Afterwards these data from all satellites were merged into one common database, while retaining the temporal resolution (1 sec) of the original data.

Further details about this processing are described by *Edwards et al.* [2017].

Measurements of the IMF and solar wind velocity from the Advanced Composition Explorer (ACE) spacecraft were processed in order to obtain values of the IEF associated with each spacecraft magnetic field measurement. Initially, the time delays of the solar wind/IMF propagation from their measurement at ACE to arrival at the Earth's bow shock were calculated, using the algorithm described by *Weimer and King* [2008]. An additional delay of 20 min was added for the time it takes for the ionosphere to respond, as determined empirically by *Weimer et al.* [2010]. Mean values are calculated at 5-min steps, using a sliding average of the values over the previous 20 minutes. The results are not very sensitive to the width of the averaging window; as shown by *Weimer et al.* [2010], the response of the ionosphere has a very broad peak when different window widths are used. These smoothed solar wind velocity and IMF values were calculated for the entire time period that spans all missions, then assigned to the nearest magnetic field sample from Ørsted, CHAMP, and the three Swarm satellites.

As mentioned earlier, the IEF is computed from the product of the solar wind velocity in the Earthward direction times the magnitude of the magnetic field in the perpendicular, Y-Z plane in GSM coordinates. The angle of the IMF in the Y-Z plane, also known as the “clock angle”, is used in our analysis. The “dipole tilt angle” associated with each measurement was computed; this angle depends on the seasonal tilt of the Earth's rotational axis with respect to the Sun, as well as the time-of-day variation of the position of the Earth's magnetic dipole axis, that rotates around the geographic spin axis.

The temporal cadence of all the data that are used is 1 s, even in cases where higher resolutions are available. Altogether, the magnetometer measurements that we used from these satellites covers the time span from 15 March 1999 through 17 August 2015 (with

a three year gap), a time period of approximately 14 years. Figure 1 is a graph of the distribution of the magnetic field measurements as a function of the IEF, for all clock angles and tilt angles. This diagram shows why the long time span is required, as there are substantially fewer cases (6.7%) where the IEF is over 4 mV/m. This level corresponds to an IMF magnitude of 8 nT with a solar wind velocity of 500 km/s.

3. Field Aligned Current Calculation

Following the removal of the internal field from the magnetic field measurements, these data are divided into 15 groups, according to the magnitude of the IEF. The divisions were arranged to contain roughly the same data counts at the low range of the IEF, with increasingly larger widths at the upper end. The bins are then further separated into eight groups by IMF clock angle and three more by dipole tilt angle, resulting in a total of 360 bins. In order to avoid samples taken with unusually low or high levels of the solar flux $F_{10.7}$ index, data taken when this index was below $90 \cdot 10^{-22} \text{Wm}^{-2} - \text{Hz}^{-1}$ or above $230 \cdot 10^{-22} \text{Wm}^{-2} - \text{Hz}^{-1}$ were excluded. The number of data samples in these bins ranged from a low of 34900 points to a high of 1001416 points, with a mean value of 474508. Even though the hemisphere locations are retained in the initial processing, the data from the Northern and Southern hemispheres were combined, with the signs of the Southern hemisphere's data reversed as needed. The combination is done in order to keep as much data as possible at the upper-most range of the IEF where the available data are very sparse, as shown in Figure 1. At the lower IEF values we have examined FAC maps produced by separating the data by hemisphere, and the results are very similar. The total FAC in the Southern hemisphere is generally about 2% to 10% less than in the

Northern hemisphere, and the differences are not enough to have a substantial influence on the results.

The two $\Delta\mathbf{B}$ components within each of the 360 bins were then used in a Spherical Cap Harmonic Analysis (SCHA) [*Haines, 1985*]

$$\Delta\mathbf{B}_n(\Lambda, \varphi) = \sum_{k=0}^{19} \sum_{m=0}^{\min(k,3)} P_{n_k(m)}^m(\cos\Lambda)(g_k^m \cos m\varphi + h_k^m \sin m\varphi) \quad (1)$$

with the coefficients g_k^m and h_k^m derived from a least-errors fit of the data. This fit is done over a polar cap having a half-angle (maximum co-latitude) Θ_0 of 45° . Λ is the co-latitude and φ is the longitude, corresponding to magnetic local time (MLT). These angles are in geomagnetic apex coordinates [*VanZandt et al., 1972; Richmond, 1995*]. As explained by *Haines [1985]*, $P_{n_k(m)}^m$ is an Associated Legendre function with integer order m . The real, non-integer degrees in this function is determined from the integers k and m , as well as Θ_0 , indicated by the notation $n_k(m)$. Only the terms corresponding to even values of $k - m$ are used.

Two examples of the results from these fits are illustrated in Figure 2, for IMF clock angles corresponding to IMF B_Y in the negative (2a) and positive (2b) directions. The two rows show the two vector components of $\Delta\mathbf{B}_n$ in the sunward and dawn-to-dusk directions.

While it is easier to use Northward and Eastward directions instead, the resulting FAC that are calculated tend to have more artificial oscillations at low latitudes. The choice of using the sunward and duskward vector component reduces these oscillations in the derived FAC.

From the results of these fits of the magnetic field perturbations, the FAC are then derived using Ampere's Law:

$$\mu_0\mathbf{J} = \nabla \times \Delta\mathbf{B} , \quad (2)$$

recalling that both components are always perpendicular to the main magnetic field.

While Hall currents within the ionosphere may produce a measurable magnetic deflection at the altitude of the CHAMP satellite, the magnetic fields from these currents have zero curl outside of the ionosphere, so they do not influence the FAC calculated by (2).

Example maps of the currents are illustrated in Figure 3, from the same data that was used for Figure 2, so that the top-left graph (3a) corresponds to (2a), and the top-right graph (3b) corresponds to (2a). The current densities are calculated on a spherical grid, and the total current within each grid cell is derived by multiplication with their surface area. The sums indicated in the upper-left and right corners in Figure 3 are obtained by totaling the currents in all grid cells that have the same sign.

4. Separation by Region Identification

As mentioned in the introductory Section 1.2, in the early work by *Iijima and Potemra* [1976] the field-aligned currents tend to be arranged in belts or regions, and the terminology R0, R1, and R2 is introduced. In the examples illustrated in Figures (3a) and (3b) these regions are labeled. It is apparent in these examples that in some cases the R1 and R2 on the dawn and dusk sides may merge together near noon and midnight, and R0 and R1 may run together near noon. It is noted that there really isn't any formal definition for where these regions begin and end in such cases, particularly for R0.

From the results of the fits for all bins, we have calculated the boundaries the the various FAC regions, and obtained the current in each region, on both the dawn and dusk sides. It was found that a flexible definition of the terms "dawn" and "dusk" is required. A numerical algorithm was developed, in which the boundary lines between these sides are automatically determined; they are placed where the absolute values of

the total current on the meridian reaches a local minimum. This method avoids use of visual inspection to place the boundaries, which would introduce a personal bias. Given the way in which these regions overlap, and the lack of a formal definition, the development of the numerical algorithm that could correctly locate the R0, R1, and R2 boundaries was much more difficult than one would assume.

We refer to *Edwards et al.* [2017] for a more description of the algorithm that was developed; results from the two examples are included in Figure 3. In (3a) and (3b) the black circles show boundaries that were determined automatically, marking the low-latitude limit of the FAC. Artifacts in the FAC that result from spherical harmonic oscillations may occur below this boundary. These artifacts are excluded from the region totals. In (3c) and (3d) are graphs of the total current in each region, as computed within meridional slices that are 1° wide. The dawn-dusk boundary lines that separate the different regions are included in both the top and bottom parts of Figure 3. The R1 currents are drawn with the solid lines in (3c) and (3d), red for the positive FAC and blue for negative. The long-dash lines represent the R2 currents, and the dotted lines show the R0. Note that amount of current across the R0–R1 and R1–R2 boundaries tends to be continuous, although this is not always the case.

5. Total currents at increasing levels of the IEF

Figure 4 shows the results for the total FAC as a function of the IEF. The total of the downward and upward currents are shown. As the downward currents need to be balanced by upward current, the totals are nearly the same, differing in magnitude only in the third decimal place. Nevertheless, the mean of their absolute values are used. The results for different IMF clock angles are shown in the eight graphs, while the three colors represent

the results for the dipole tilt angles that correspond to summer-like conditions (red), equinox (green), and winter (blue). The crosses show the data points, using the mean value of the IEF for each bin on the horizontal axis, and the total current on the vertical axis. The shaded boxes indicate the standard deviations in both directions. The solid lines show the results from a linear, least-error-fit of these data, taking into consideration the standard deviations in both directions, using an algorithm adopted from “*fitexy*” by Press *et al.* [1994]. The IMF is more likely to be oriented at the 90° and 270° clock angle than purely southward. This is the reason for the larger errors at 180°.

As each point on the graph is derived from SCHA fits of collection of data points, that were selected according to the IEF and other parameters being within a specified range, it is a simple matter to calculate the standard deviation of the IEF values associated with each fit. The standard deviations along the abscissa get progressively larger since the bins needed to have a wider range as the IEF values increase, in order to collect a sufficient number of points for a good fit. This increasing bin width follows from the trend shown in Figure 1.

Along the ordinate, the calculation of the standard deviation is not so simple. When the maps of the two $\Delta\mathbf{B}_n$ components are derived from fitting, as shown in Figure 2, the errors and standard deviations of the results are calculated with each fit. These values, in units of nT, do not easily translate to errors in the resulting FAC maps, after application of (2). In statistics there are definitions of “relative standard error” and “relative standard deviation,” the later defined as the percentage that results from dividing the standard deviation of a sample by the mean value of the sample. This won’t work for our case since the means in the $\Delta\mathbf{B}_n$ maps may be close to zero, and don’t correlate to the FAC. On

the other hand, the strength of the FAC are directed related to the difference between the maximum and minimum values in these maps, in the sunward component in particular. Dividing the standard deviation from the fitting of $\Delta\mathbf{B}_n$ sunward by the difference between the maximum and minimum values results in a dimensionless percentage. Multiplying the total FAC by this percentage provides a measure of the standard deviation for this FAC, in the same units. While this method is only an approximation of the standard deviations in the FAC, it is how the ordinate errors are calculated.

Even without the lines that are drawn in Figure 4, it is obvious that the total FAC keeps increasing as the IEF increases, with no clear indication of leveling off. Recalling that in the electric potential studies, the roll-over to the more constant levels occurs by the time the IEF is in the range of 3 to 5 mV/m [Shepherd, 2007; Wilder *et al.*, 2008]. The results that we obtained go well beyond this level, without much indication that the slopes in the total FAC as a function of the IEF changes very much. The “*fitexy*” algorithm provides the probability that the data match a linear model, taking the standard deviations in both directions into consideration. In the results shown in Figure 4 the greater majority of the probabilities were 1., with the lowest being 0.998. It is also noteworthy that the trend persists for all clock angles, even for Northward IMF, 0° clock angle.

So the next question is how do the R1 currents behave? We are able to show this, due to the effort taken to obtain the total current in the different regions. While it is possible to graph only the R1, in Figure 5 are shown the totals of the R1 plus the connected R0 that have the same sign. These currents often have no apparent dawn–dusk separation other than where the lines are drawn. The positive R1 on the dawn side is added with the connected, positive R0 on the dusk side. Likewise, the current in the dusk R1 is added

with the dawn R0. Using absolute values, the mean value of the dawn and dusk R1+R0 totals are plotted. These results are the same as before, so it is obvious that these currents have the same linear behavior, showing few signs of saturation. A graph with only R1 (not shown) shows very similar results.

As the Region 2 currents could have a role in the electric potential saturation, we look at this possibility next. For example, if more current from R1 starts to flow directly to the adjacent R2, without crossing the polar cap, then that could in principle reduce the electric fields and potential difference. In Figure 6 are shown the total, transpolar current as a function of the IEF. These values are computed on each of the dawn and dusk sides by adding together the Regions 0, 1 and 2 that are located on the same side of the boundary lines. As R0 and R2 have signs that are opposite of R1, they subtract from the total R1. The result is the amount of current that needs to flow across the dawn–dusk boundary in the polar cap, connecting the R1 on each side. As in the other graphs, Figure 6 shows the mean, absolute values from both sides. The results are the same as before, with no apparent change in the slope as the IEF increases. If there was any change in the relative amount of current going between R1 and R2, then there would have been a variation in the slope.

6. Clock Angle Variations of Current Regions

Since we now have the capability to determine the total current associated with each of the different regions, it is possible to examine the behavior of the various regions as function of the IMF clock angle. The results of these calculations are shown in Figure 7. All data were obtained when the IEF was in the range of 3.1 – 3.8 mV/m, the center

being 3.45 mV/m. As before, the results are shown for all three groups of dipole tilt angle, corresponding to summer (red), equinox (green), and winter (blue) conditions.

Figure 7(a) shows only the total R0 currents, positive on the dusk side, which reach their maximum values at IMF clock angles 90° on the dawn side and 270° on the dusk side. For this reason the R0 currents are often referred to as the “ B_Y ” current system, although the evolution of these R0 currents into the “NBZ” system is also apparent. The R0 currents are basically absent at 180° clock angle. To further illustrate these changes, Figure 8 contains the maps of the FAC at eight clock angles for the summer tilt angle conditions.

The Region 1 totals are shown in 7(b). There is some asymmetry with respect to the 180° clock angle, with the positive current peaking at lower clock angles and the negative Region 1 current peaking at clock angles greater than 180° . When the R0 current that has the same sign is added, as in 7(d), the symmetry is more balanced.

Figure 7(c) shows that the Region 2 currents tend to track the changes in the R1 currents, although at lower magnitudes. For example, the largest positive R1 and the most negative R2 totals are both found at 135° clock angle, and the R1 and R2 currents having the opposite signs peak at 180° clock angle. One puzzling result found in 7(c) is that the positive R2 currents on the dusk side tend to have larger sums in winter and equinox than the summer, particularly for clock angles under 225° ; in the majority of cases the summer currents are greatest.

The behavior of the transpolar currents, the Region 1 minus the Region 0 and 2 on each side, are shown in 7(e). These always peak at 180° clock angle, and may actually reverse signs at 0° clock angle due to the strong R0 system. Not surprisingly, the results in 7(e)

are in general agreement with how the the cross-polar cap electric potentials vary with clock angle, as shown by *Weimer* [1995].

Finally, 7(f) shows the totals of all positive (downward) and negative (upward) current, without any regard for region/location. These totals are well-ordered by the season and dipole tilt angle, largest in the summer and smallest in the winter.

7. Discussion

Our results indicate the the total amount of field-aligned current does not seem to saturate in response to the level of the interplanetary electric field. This is quite certain up to IEF values of 10 mV/m, which is more than double where the electric potentials saturate. These results are similar to those found by *Anderson and Korth* [2007], although we find that the FAC continue to increase rather than leveling off. A similar result for the total duskward current was found recently by *Zhou and Lühr* [2017], using magnetometer measurements from CHAMP, for “merging electric field” values up to 6 mV/m.

The lack of an obvious saturation is found for all IMF clock angles and all current regions. At more extreme levels of driving the number of such events are so sparse that it is difficult to provide an unequivocal determination whether or not the total current does level off at some point. Below 7 mV/m linear trends are found at all IMF clock angles, and up to 15 mV/m the mean values still follow a linear slope for cases where the Z component of the IMF is zero or positive. Interestingly, it is only for the southward IMF cases where the data points at 10 mV/m and greater tend to lie below the linear regression curve, as one referee had pointed out. This reviewer suggested that this behavior may be related to the response of the R1 and transpolar currents during different phases of geomagnetic

storm periods, and that a different response might be found before and after the build up of ring current.

By dividing and summing the amount of the FAC by region, it was possible to find how much of the Region 1 goes into the Region 0 and Region 2 on each side of the dawn-dusk boundary. The remainder of the current needs to cross the dawn-dusk boundary, so this is called the transpolar current, flowing from dawn toward dusk. This transpolar current also has a linear slope for all IMF clock angles, indicating that at each angle the ratio between the amount of current in each region remains the same; at 180° clock angle Region 2 closes approximately 56% of the Region 1 current, and 44% crosses the polar cap, closing with the other Region 1. As mentioned earlier, the variations in the transpolar current as a function of the clock angle, as shown in Figure 7(e), have the same behavior as the electric potentials.

These results indicate that the source of the currents acts more like a current generator rather than a voltage generator. The saturation theories of *Ridley* [2007] and *Lopez et al.* [2008] remain as viable explanations for the saturation of the electric potentials. On the other hand, since the transpolar current keeps going up while the electric potentials do not, then it seems that the conductivity in the ionosphere must be increasing. This may be the only explanation that is needed, as satellite measurements of particle precipitation indicate that the conductivity increases with the level of geomagnetic activity [*Fuller-Rowell and Evans*, 1987; *Hardy et al.*, 1987; *Ahn et al.*, 1998]. The relationship between the transpolar current and electric potential is not so simple, as when the auroral oval expands this current is spread out along a larger distance that is perpendicular to the current flow, meaning that the electric field may not necessarily increase linearly with the

current. Expansion of the oval also causes the integration distance between the electric field reversals to increase.

In almost all cases the FAC are larger in the summer hemisphere than in the winter. A similar result was found by *Coxon et al.* [2016], *Zhou and Lühr* [2017], and *Edwards et al.* [2017]. A current generator source is consistent with this finding; since the summer and winter hemispheres are connected in parallel, with roughly the same voltages, it is reasonable that more current flows to where the conductivity is higher.

The recently developed process for identifying and totaling the FAC by region has been found to be very useful, as shown in the results in Figures 7 and 8. The dividing line between the dawn and dusk sides is determined numerically, rather than using manual choices that could be biased. These divisions are marked where all current along a meridian reaches a minimum, using the total of absolute values. The method finds the obvious boundaries where there are gaps in the R1 and R2 currents. In other cases these regions connect with each other through noon or midnight, and a visual placement of the boundary isn't clear, yet the algorithm is consistent in boundary placement; the boundaries are the same in maps that use different, non-overlapping data. As found in several previous studies [*Ganushkina et al.*, 2015], the formation of the Region 0 currents depends on the magnitude of IMF in the GSM Y and +Z directions.

8. Summary

This investigation focused on how the field-aligned currents respond to driving by the solar wind, formulated in terms of the IEF, from the product of the solar wind velocity and magnitude of the IMF in the transverse direction. In order to obtain sufficient measurements at IEF levels where the electric potentials are observed to saturate, we use nearly 14

years of measurements combined from the Ørsted, CHAMP, and Swarm missions. After removal of Earth's internal field, the data are grouped together and fit using the SCHA technique. The current is calculated from the curl of the magnetic perturbations. As it is useful to know how the current maps in each region, we have used a recently developed algorithm to divide the FAC into the traditionally-named R0, R1, and R2.

The results show that the FAC have a linear response to the magnitude of the interplanetary electric field. No saturation of the currents is observed in any region, or the total current that crosses the polar cap. It is certain that the FAC have no sharp decrease in their slope up to IEF levels of 10 mV/m, which is more than double the level where the electric potentials have an obvious roll-over in their slope. At higher IEF levels a linear trend appears to continue, particularly for conditions where the Z component of the IMF is zero or greater. When IMF B_Z is negative there may be a slight reduction in the FAC at 10 mV/m and greater, although there is less certainty in this range due to the scarcity of data.

The total FAC is always higher in the summer hemisphere than the winter hemisphere. The results indicate that the flow of the solar wind and its magnetic field around the magnetosphere acts as a current source. The non-linear trend observed in the electric potentials may result if the ionospheric conductivity increases as the level of driving increases.

Acknowledgments.

This work is supported by National Science Foundation grants AGS-1303116 and AGS-1638270 to Virginia Tech. The CHAMP mission was sponsored by the Space Agency of the German Aerospace Center (DLR) through funds of the Federal Ministry of Economics

and Technology. The Swarm mission is sponsored by the European Space Agency. We thank Hermann Lühr for fruitful discussions.

The Ørsted data are provided by the National Space Institute at the Technical University of Denmark (DTU Space) and freely available at <ftp://ftp.spacecenter.dk/data/magnetic-satellites/Orsted/>. The CHAMP data are available from the Information System and Data Center for Geoscientific Data, at GFZ German Research Centre for Geosciences, which is available at <http://isdc-old.gfz-potsdam.de/>. Swarm data were obtained from the European Space Agency, available at <https://earth.esa.int/web/guest/missions/esa-operational-eo-missions/swarm>. The level 2 ACE data can be obtained from the NASA archives at https://cdaweb.gsfc.nasa.gov/sp_phys/data/ace/ or <ftp://cdaweb.gsfc.nasa.gov/pub/data/ace>.

References

- Ahn, B.-H., A. D. Richmond, Y. Kamide, H. W. Kroehl, B. A. Emery, O. de la Beaujardiere, and S.-I. Akasofu (1998), An ionospheric conductance model based on ground magnetic disturbance data, *J. Geophys. Res.*, *103*(A7), 14,769–14,780, doi:10.1029/97JA03088.
- Anderson, B., and H. Korth (2007), Saturation of global field aligned currents observed during storms by the iridium satellite constellation, *Journal of Atmospheric and Solar-Terrestrial Physics*, *69*(1–2), 166 – 169, doi:<https://doi.org/10.1016/j.jastp.2006.06.013>.
- Anderson, B. J., H. Korth, C. L. Waters, D. L. Green, and P. Stauning (2008), Statistical Birkeland current distributions from magnetic field observations by the Iridium constellation, *Ann. Geophys.*, *26*, 671–687, doi:10.5194/angeo-26-671-2008.

Borovsky, J. E., B. Lavraud, and M. M. Kuznetsova (2009), Polar cap potential saturation, dayside reconnection, and changes to the magnetosphere, *J. Geophys. Res.*, *114*, doi:10.1029/2009JA014058.

Christiansen, F., V. O. Papitashvili, and T. Neubert (2002), Seasonal variations of high-latitude field-aligned currents inferred from Ørsted and Magsat observations, *J. Geophys. Res.*, *107*, 1029–1045, doi:10.1029/2001JA900104.

Coxon, J. C., S. E. Milan, J. A. Carter, L. B. N. Clausen, B. J. Anderson, and H. Korth (2016), Seasonal and diurnal variations in AMPERE observations of the birkeland currents compared to modeled results, *J. Geophys. Res. Space Physics*, *121*, 4027–4040, doi:10.1002/2015JA022050.

Edwards, T. R., D. R. Weimer, W. K. Tobiska, and N. Olsen (2017), Field-aligned current response to solar indices, *J. Geophys. Res. Space Physics*, *122*, 5798–5815, doi:10.1002/2016ja023563.

Friis-Christensen, E., Y. Kamide, A. D. Richmond, and S. Matsushita (1985), Interplanetary magnetic field control of high-latitude electric fields and currents determined from Greenland magnetometer data, *J. Geophys. Res.*, *90*, 1325, doi:10.1029/JA090iA02p01325.

Friis-Christensen, E., H. Lühr, and G. Hulot (2006), Swarm: A constellation to study the Earth's magnetic field, *Earth, Planets and Space*, *58*(4), 351–358, doi:10.1186/BF03351933.

Fuller-Rowell, T. J., and D. S. Evans (1987), Height-integrated Pedersen and Hall conductivity patterns inferred from the TIROS-NOAA satellite data, *J. Geophys. Res.*, *92*(A7), 7606–7618.

- Ganushkina, N. Y., M. W. Liemohn, S. Dubyagin, I. A. Daglis, I. Dandouras, D. L. De Zeeuw, Y. Ebihara, R. Ilie, R. Katus, M. Kubyshkina, S. E. Milan, S. Ohtani, N. Ostgaard, J. P. Reistad, P. Tenfjord, F. Toffoletto, S. Zaharia, and O. Amariutei (2015), Defining and resolving current systems in geospace, *Ann. Geophys.*, *33*(11), 1369–1402, doi:10.5194/angeo-33-1369-2015.
- Green, D. L., C. L. Waters, B. J. Anderson, H. Korth, and R. J. Barnes (2006), Comparison of large-scale Birkeland currents determined from Iridium and SuperDARN data, *Ann. Geophys.*, *24*, 941–959, doi:10.5194/angeo-24-941-2006.
- Green, D. L., C. L. Waters, B. J. Anderson, and H. Korth (2009), Seasonal and interplanetary magnetic field dependence of the field-aligned currents for both Northern and Southern hemispheres, *Ann. Geophys.*, *27*, 1701–1715, doi:10.5194/angeo-27-1701-2009.
- Haines, G. V. (1985), Spherical cap harmonic analysis, *J. Geophys. Res.*, *90*(B3), 2583, doi:10.1029/JB090iB03p02583.
- Hardy, D. A., M. S. Gussenhoven, R. Raistrick, and W. J. McNeil (1987), Statistical and functional representations of the patterns of auroral energy flux, number flux, and conductivity, *J. Geophys. Res.*, *92*, 12,275.
- Hill, T. W., A. Dessler, and R. A. Wolf (1976), Mercury and Mars: The role of ionospheric conductivity in the acceleration of magnetospheric particles, *Geophys. Res. Lett.*, *3*, 429, doi:10.1029/GL003i008p00429.
- Iijima, T., and T. A. Potemra (1976), The amplitude distribution of field aligned currents at northern high latitudes observed by Triad, *J. Geophys. Res.*, *81*, 2165–2174, doi:10.1029/JA081i013p02165.

Iijima, T., and T. Shibaji (1987), Global characteristics of northward IMF-associated (NBZ) field-aligned currents, *J. Geophys. Res.*, *92*, 2408–2424, doi:10.1029/JA092iA03p02408.

Iijima, T., T. A. Potemra, L. J. Zanetti, and P. F. Bythrow (1984), Large-scale Birkeland currents in the dayside polar region during strongly northward IMF: A new Birkeland current system, *J. Geophys. Res.*, *89*, 7441, doi:10.1029/JA089iA09p07441.

Kivelson, M. G., and A. Ridley (2008), Saturation of the polar cap potential: Inference from Alfvén wing arguments, *J. Geophys. Res.*, *113*, doi:10.1029/2007JA012302.

Korth, H., B. J. Anderson, J. M. Ruohoniemi, H. U. Frey, C. L. Waters, T. J. Immel, and D. L. Green (2008), Global observations of electromagnetic and particle energy flux for an event during northern winter with southward interplanetary magnetic field, *Ann. Geophys.*, *26*, 1415–1430, doi:10.5194/angeo-26-1415-2008.

Lopez, R. E., S. Hernandez, K. Hallman, R. Valenzuela, J. Seiler, P. C. Anderson, and M. R. Hairston (2008), Field-aligned currents in the polar cap during saturation of the polar cap potential, *J. Atmos. Solar-Terr. Phys.*, *70*, doi:10.1016/j.jastp.2007.08.072.

Lu, G., L. R. Lyons, P. H. Reiff, W. F. Denig, O. de la Beaujardiere, H. W. Kroehl, P. T. Newell, F. J. Rich, H. Opgenoorth, M. A. L. Persson, J. M. Ruohoniemi, E. Friis-Christensen, L. Tomlinson, R. Morris, G. Burns, and A. McEwin (1995), Characteristics of ionospheric convection and field-aligned current in the dayside cusp region, *J. Geophys. Res.*, *100*, 11,845, doi:10.1029/94JA02665.

Maus, S. (2007), CHAMP magnetic mission, in *Encyclopedia of geomagnetism and paleomagnetism*, edited by D. Gubbins and E. Herrero-Bervera, pp. 59–60, Springer, Heidelberg.

Olsen, N. (2007), Ørsted, in *Encyclopedia of geomagnetism and paleomagnetism*, edited by D. Gubbins and E. Herrero-Bervera, pp. 743–745, Springer, Heidelberg.

Olsen, N., E. Friis-Christensen, R. Floberghagen, and *et al.* (2013), The Swarm satellite constellation application and research facility (SCARF) and Swarm data products, *Earth, Planets and Space*, *65*(1), 1189–1200, doi:10.5047/eps.2013.07.001.

Papitashvili, V. O., F. Christiansen, and T. Neubert (2002), A new model of field-aligned currents derived from high-precision satellite magnetic field data, *Geophys. Res. Lett.*, *29*, doi:10.1029/2001GL014207.

Press, W. H., S. A. Teukolsky, W. T. Vetterling, and B. P. Flannery (1994), *Numerical Recipes in C: The Art of Scientific Computing, Second Edition*, second ed., Cambridge Univ. Press, New York.

Reigber, C. H., H. Lühr, and P. Schwintzer (2002), Champ mission status, *Advances in Space Research*, *30*(2), 129–134, doi:10.1016/S0273-1177(02)00276-4.

Richmond, A. D. (1995), Ionospheric electrodynamics using magnetic apex coordinates, *J. Geomag. Geoelectr.*, *47*, 191, doi:10.5636/jgg.47.191.

Ridley, A. J. (2007), Alfvén wings at Earth’s magnetosphere under strong interplanetary magnetic fields, *Ann. Geophys.*, *25*, 533, doi:10.5194/angeo-25-533-2007.

Shepherd, S. G. (2007), Polar cap potential saturation: Observations, theory, and modeling, *J. Atmos. Solar-Terr. Phys.*, *69*, 234, doi:10.1016/j.jastp.2006.07.022.

Siscoe, G., J. Raeder, and A. J. Ridley (2004), Transpolar potential saturation models compared, *J. Geophys. Res.*, *109*, A09,203, doi:10.1029/2003JA010318.

Siscoe, G. L., G. M. Erickson, B. U. Ö. Sonnerup, N. C. Maynard, J. A. Schoendorf, K. D. Siebert, D. R. Weimer, W. W. White, and G. R. Wilson (2002a), Hill model of

transpolar potential saturation: Comparisons with MHD simulations, *J. Geophys. Res.*, *107*(A6), 1075, doi:10.1029/2001JA000109.

Siscoe, G. L., N. U. Crooker, and K. D. Siebert (2002b), Transpolar potential saturation: Roles of the region 1 current system and solar wind ram pressure, *J. Geophys. Res.*, *107*(A10), doi:10.1029/2001JA009176.

Stauning, P. (2002), Field-aligned ionospheric current systems observed from Magsat and Oersted satellites during northward IMF, *Geophys. Res. Lett.*, *29*, 8005–8008, doi:10.1029/2001GL013961.

Sundberg, K. Å. T., J. A. Cumnock, and L. G. Blomberg (2009), Reverse convection potential: A statistical study of the general properties of lobe reconnection and saturation effects during northward IMF, *J. Geophys. Res.*, *114*, doi:10.1029/2008JA013838.

Thomsen, P. L., and F. Hansen (1999), Danish Ørsted mission in-orbit experiences and status of the danish small satellite programme, in *13th Annual AIAA/Utah State University Conference on Small Satellites*, Logan, UT.

VanZandt, T. E., W. L. Clark, and J. M. Warnock (1972), Magnetic apex coordinates: A magnetic coordinate system for the ionospheric f_2 layer, *J. Geophys. Res.*, *77*, 2406, doi:10.1029/JA077i013p02406.

Waters, C. L., B. J. Anderson, and K. Liou (2001), Estimation of global field aligned currents using the Iridium system magnetometer data, *Geophys. Res. Lett.*, *28*, 2165, doi:10.1029/2000GL012725.

Weimer, D. (1995), Models of high-latitude electric potentials derived with a least error fit of spherical harmonic coefficients, *J. Geophys. Res.*, *100*, 19,595, doi:10.1029/95JA01755.

Weimer, D. (2000), A new technique for the mapping of ionospheric field-aligned currents from satellite magnetometer data, *in Magnetospheric Current Systems, Geophys. Monogr. Ser. 118*, pp 381–388, doi:10.1029/GM118p0381.

Weimer, D. (2001), Maps of field-aligned currents as a function of the interplanetary magnetic field derived from Dynamic Explorer 2 data, *J. Geophys. Res.*, *106*, 12,889, doi:10.1029/2000JA000295.

Weimer, D. R. (2005), Predicting surface geomagnetic variations using ionospheric electrodynamic models, *J. Geophys. Res.*, *110*, A12307, doi:10.1029/2005JA011270.

Weimer, D. R., and J. H. King (2008), Improved calculations of interplanetary magnetic field phase front angles and propagation time delays, *J. Geophys. Res.*, *113*, A01105, doi:10.1029/2007JA012452.

Weimer, D. R., C. R. Clauer, M. J. Engebretson, T. L. Hansen, H. Gleisner, I. Mann, and K. Yumoto (2010), Statistical maps of geomagnetic variations as a function of the interplanetary magnetic field, *J. Geophys. Res.*, *115*, A10320, doi:10.1029/2010JA015540.

Wilder, F. D., C. R. Clauer, and J. B. H. Baker (2008), Reverse convection potential saturation during northward IMF, *Geophys. Res. Lett.*, *35*, doi:10.1029/2008GL034040.

Wilder, F. D., C. R. Clauer, and J. B. H. Baker (2009), Reverse convection potential saturation during northward IMF under various driving conditions, *J. Geophys. Res.*, *114*, doi:10.1029/2009JA014266.

Zanetti, L. J., T. A. Potemra, T. Iijima, W. Baumjohann, and P. F. Bythrow (1984), Ionospheric and Birkeland current distributions for northward interplanetary magnetic field: Inferred polar convection, *J. Geophys. Res.*, *89*, 7453, doi:10.1029/JA089iA09p07453.

Zhou, Y.-L., and H. Lühr (2017), Net ionospheric currents closing field-aligned currents in the auroral region: CHAMP results, *J. Geophys. Res. Space Physics*, *122*, 4436–4449, doi:10.1002/2016JA023090.

Accepted Article

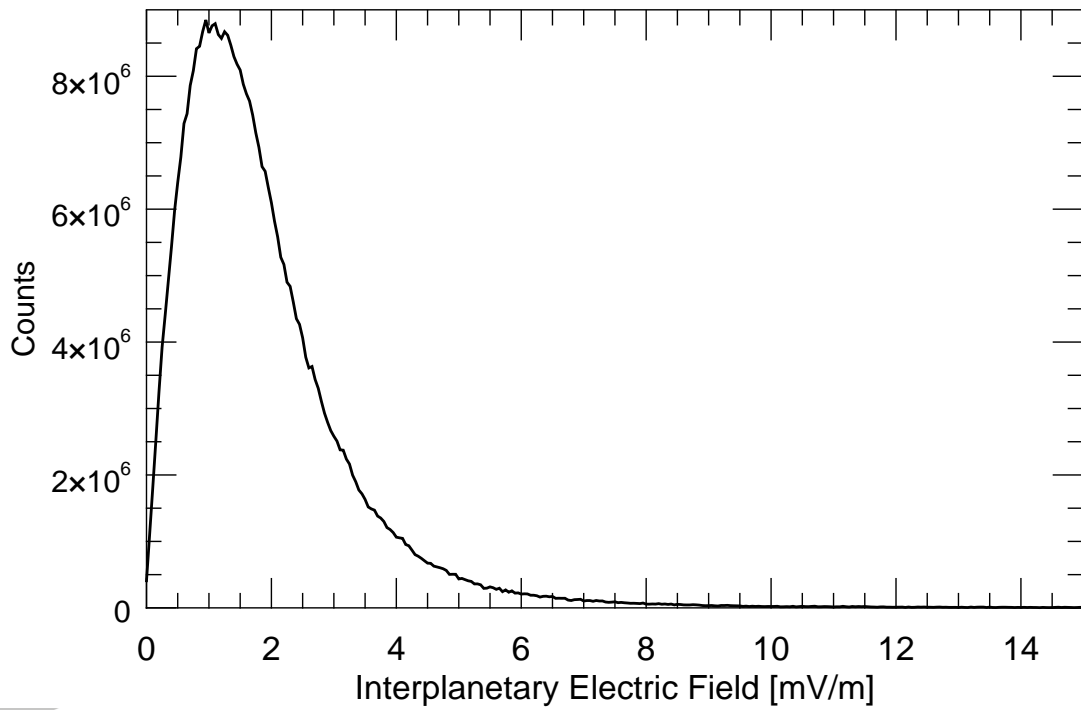


Figure 1. Distribution of magnetometer measurements as a function of the interplanetary electric field. The counts are the number magnetic field measurements, from the Ørsted, CHAMP, and Swarm satellites, falling within each interval that spans at width of 0.05 mV/m, as computed from the solar wind and IMF measurements from the ACE satellite.

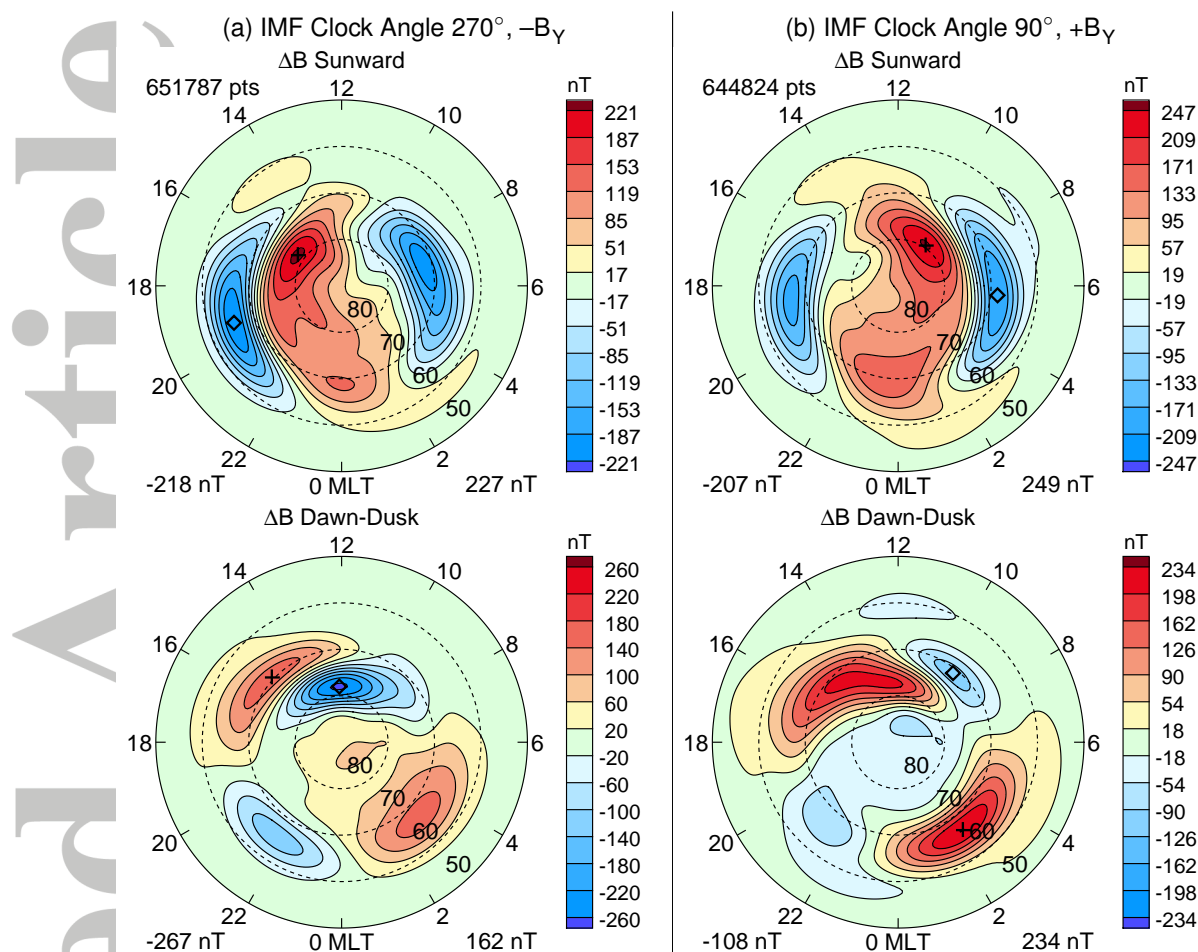


Figure 2. Examples of magnetic field perturbations, for two IMF orientations. Derived from SCHA fits from data taken when the SWE was in the range of 3.8 to 5 mV/m, (a) shows the results for IMF in the GSM -Y direction (IMF clock angle $270^\circ \pm 22.5^\circ$), and (b) shows the results IMF in the GSM +Y direction (IMF clock angle $90^\circ \pm 22.5^\circ$). The dipole tilt angle was $0^\circ \pm 12^\circ$. The upper maps show the vector component in the sunward direction, and the lower row shows the vector component in the dawn-to-dusk direction. The total number of data points used in each fit is indicated in the upper-left corner, while the minimum and maximum values are shown in the lower-left and right corners of each map.

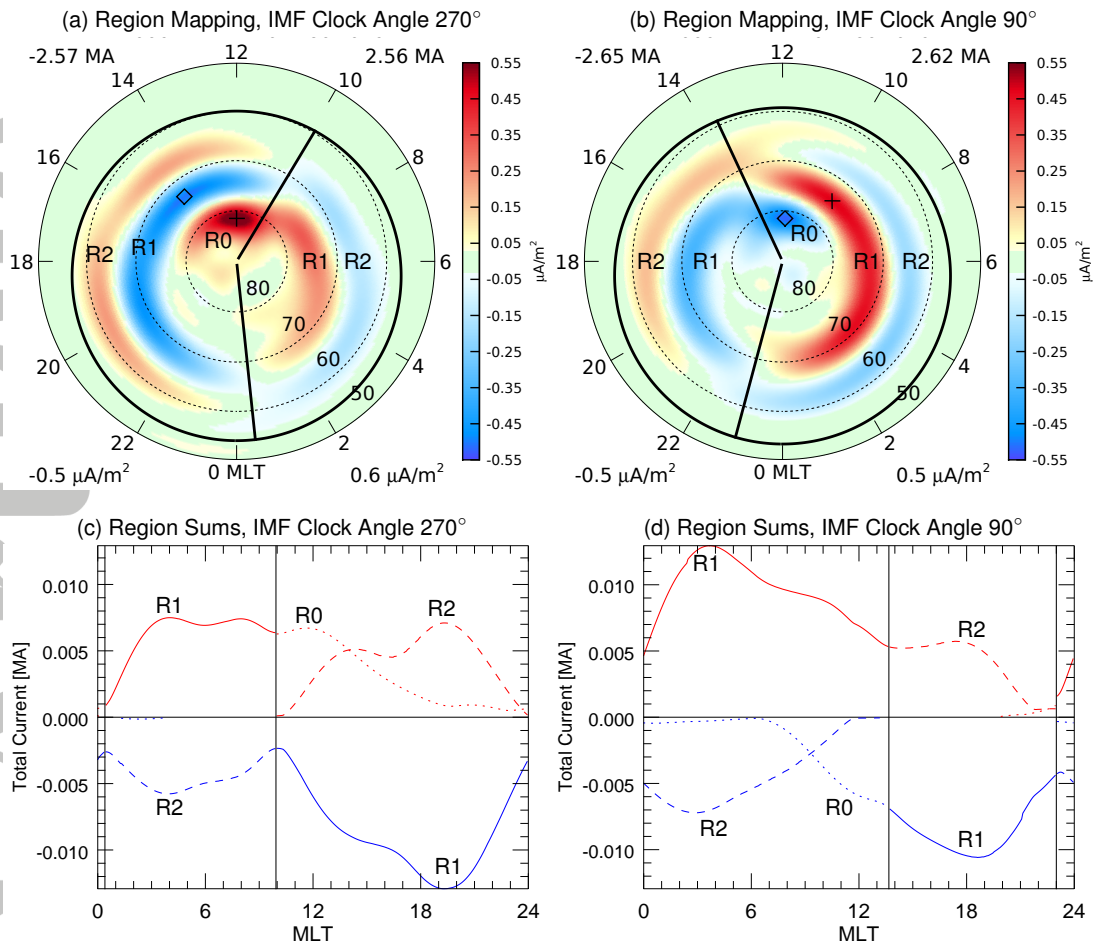


Figure 3. Field-aligned currents and region identification. The field-aligned currents maps for (a) IMF clock angle 270° , and (b) IMF clock angle 90° , were derived from the magnetic perturbations presented in Figure 2. The total amount of upward and downward currents are indicated in the upper-left and right corners, while the minimum and maximum FAC intensity are in the lower-left and right corners. The black circle indicates the bounding latitude for determining the sums in each region, indicated by the R0, R1, and R2 labels. The black meridian line indicate the divisions between the “dawn” and “dusk” sides. Graphs (c) and (d) show the total amount of current within each degree of longitude that was found within each region. The positive currents are drawn in red, while the negative currents are drawn in blue.

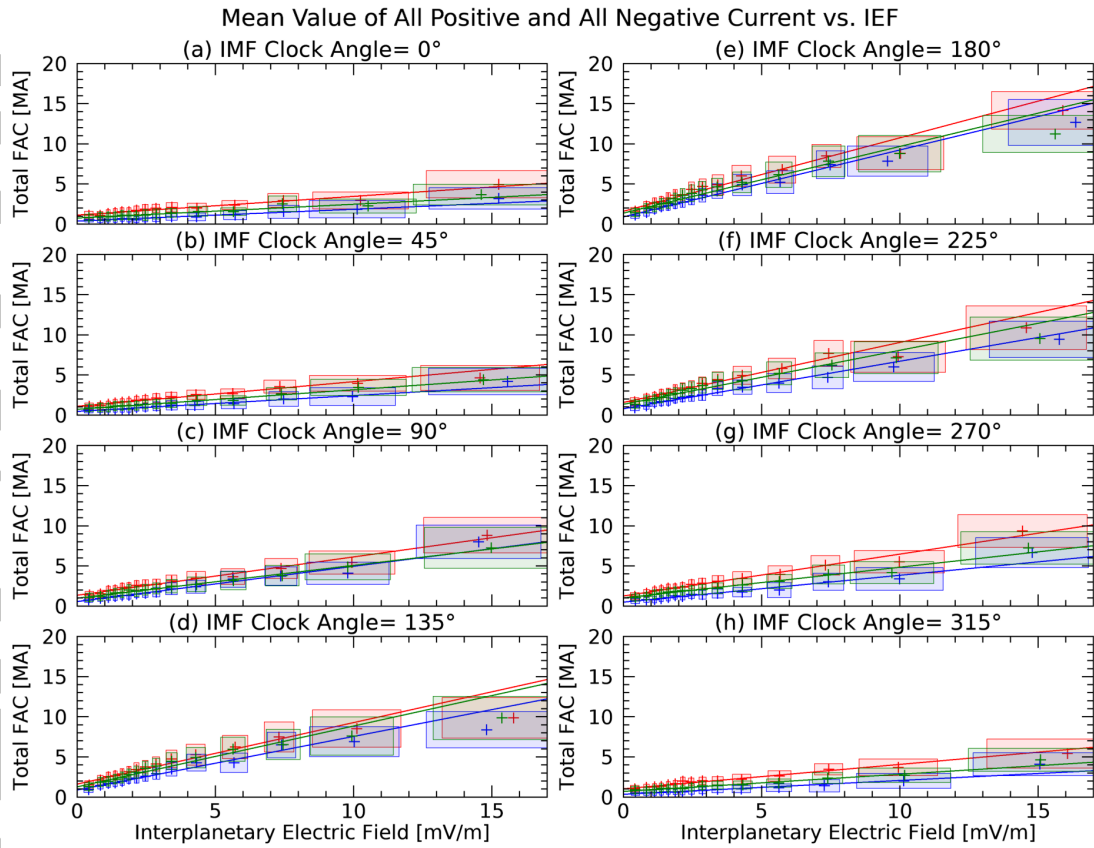


Figure 4. Total FAC vs. IEF. The total downward and upward currents, the mean of the absolute values on each side, shown as a function of the IEF. Each panel shows the results for one IMF clock angle, with the tilt angle variations superposed, with the red lines representing the results corresponding to summer, green for equinox, and blue for winter.

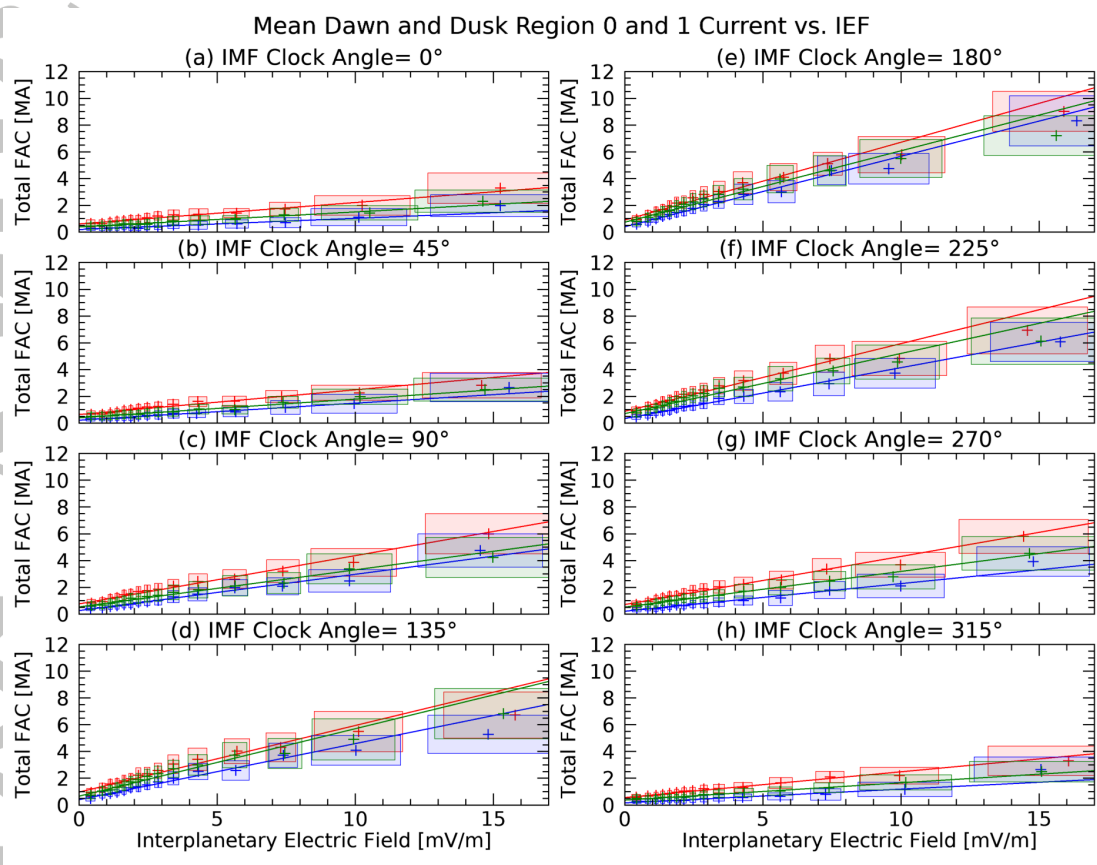


Figure 5. Total R1 FAC vs. IEF. The total Region 1 plus Region 0 currents, using the mean of the absolute values on each side, shown as a function of the IEF. Each panel shows the results for one IMF clock angle, with the tilt angle variations superposed, with the red lines representing the results corresponding to summer, green for equinox, and blue for winter.

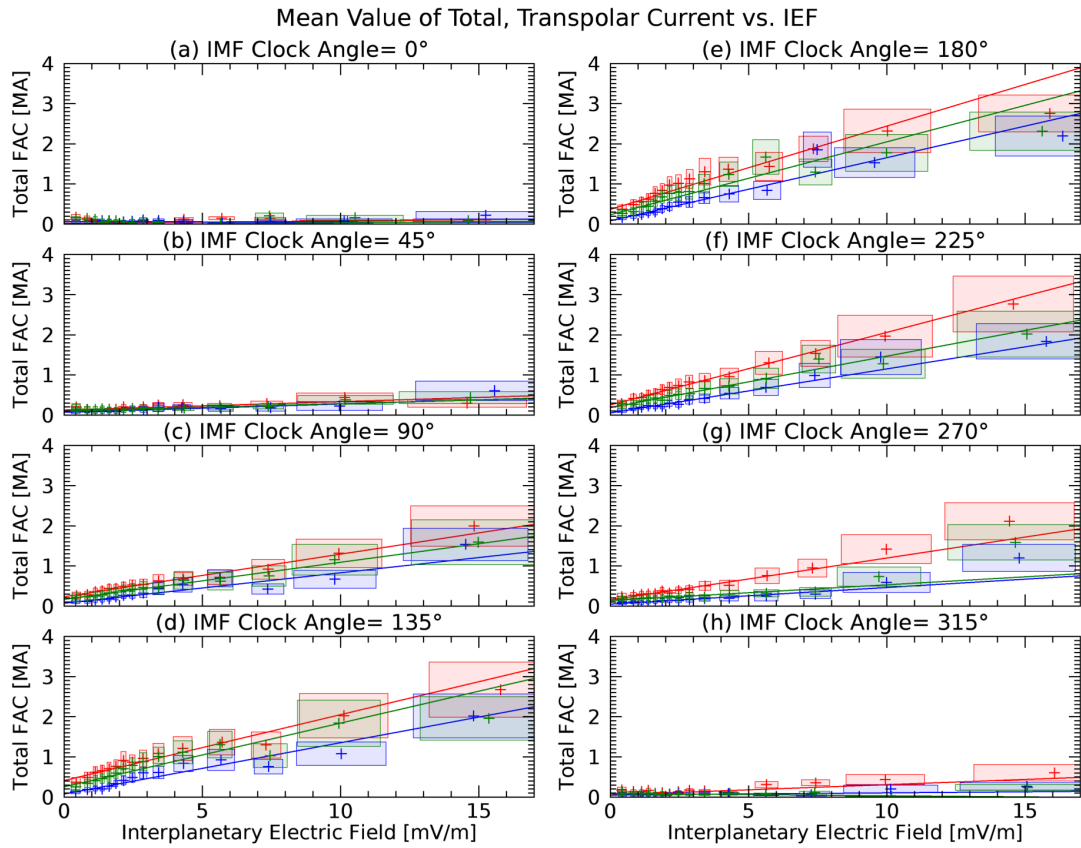


Figure 6. Total transpolar current vs. IEF. The total of of the Regions 0, 1 and 2 currents are shown, the amount of current crossing the polar cap. Each panel shows the results for one IMF clock angle, with the tilt angle variations superposed, with the red lines representing the results corresponding to summer, green for equinox, and blue for winter.

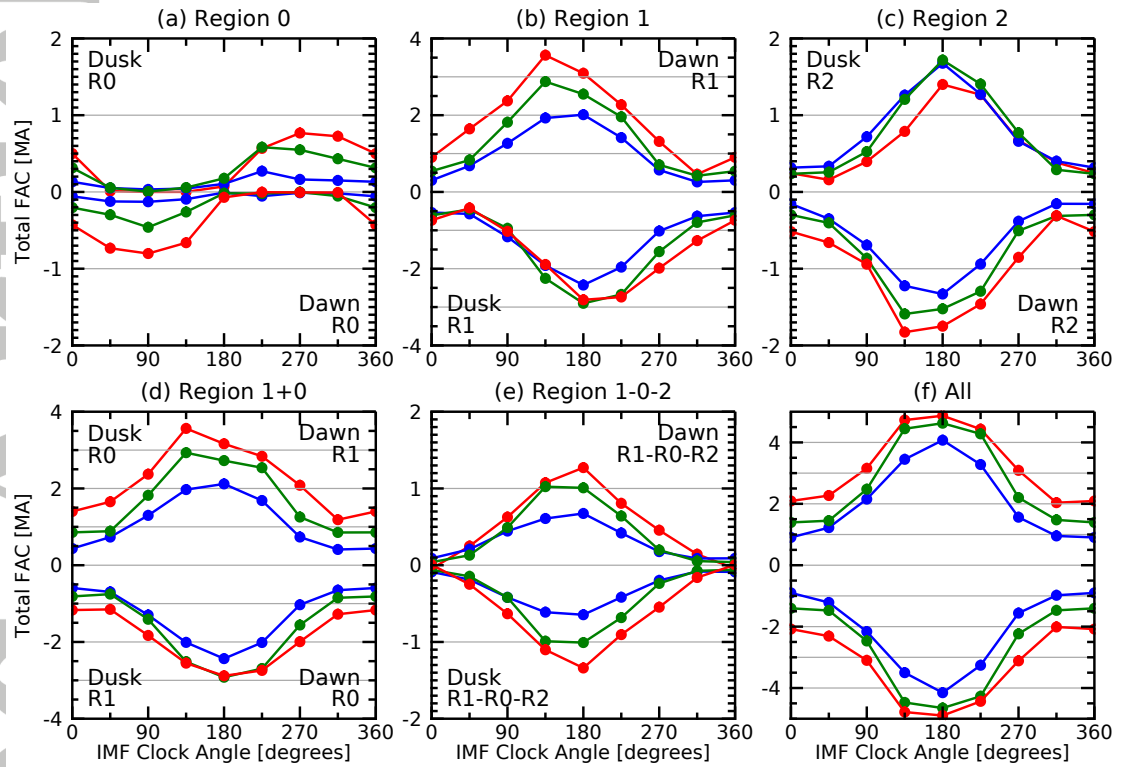


Figure 7. Total current as a function of IMF clock angle. (a) Region 0, positive on the dusk side. (b) Region 1, positive on the dawn side. (c) Region 2, positive on the dusk side. (d) Sum of Region 1+0, that have the same sign when crossing the dawn–dusk boundary. (e) Sum of Regions 0, 1, and 2 on each side, with R0 and R2 both subtracting from R1. (f) Total of all upward and downward current. The red lines show results for dipole tilt angles corresponding to summer, green represent equinox, and blue correspond to winter.

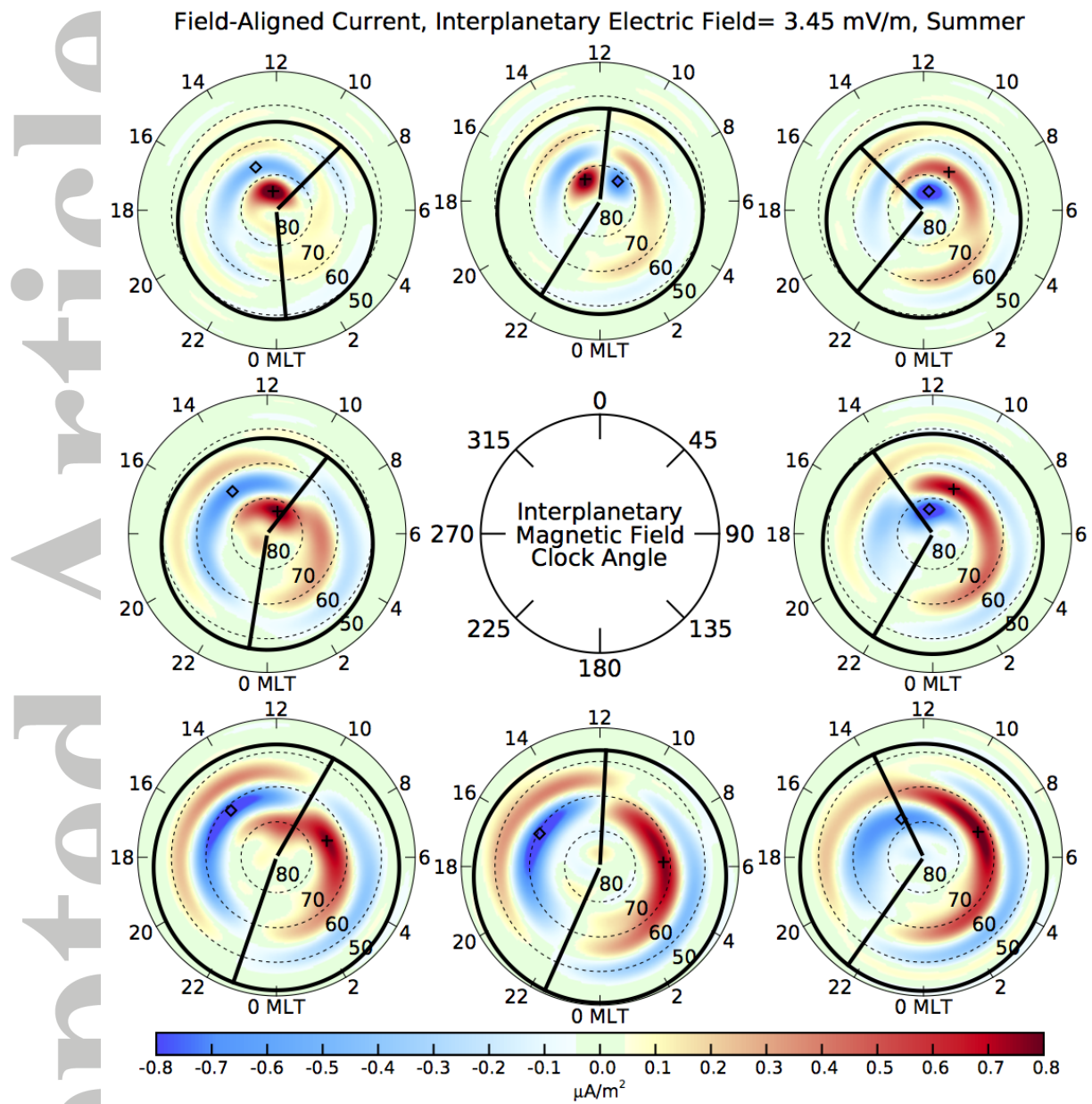


Figure 8. Maps of the field-aligned current intensity at eight IMF clock angles, and indicated in the center, for summer tilt conditions and mean IEF of 3.45 mV/m. The black meridian line indicate the divisions between the “dawn” and “dusk” sides, while the circular line indicates the low-latitude boundary from the Region identification algorithm.